Combining high X-ray energy photon-in photon-out spectroscopies and X-ray scattering to experimentally assess the emergence of electronic- and atomic structure of ZnS nanorods

Lars Klemeyer,[1] *Tjark L. R. Gröne,*[1] *Cecilia de Almeida Zito,*[1] *Olga Vasylieva,*[1] *Melike Gumus Akcaalan,*[1] *Sani Y. Harouna-Mayer,*[1,2] *Francesco Caddeo,*[1] *Torben Steenbock,*[3] *Sarah-Alexandra Hussak,*[1] *Jagadesh Kopula Kesavan,*[1] *Ann-Christin Dippel,*[4] *Xiao Sun,*[4] *Andrea Köppen,*[5] *Viktoriia A. Saveleva,*[6] *Surender Kumar,*[3] *Gabriel Bester,*[2,3] *Pieter Glatzel,*[6] *and Dorota Koziej*[1,2*]

[1] University of Hamburg, Institute for Nanostructure and Solid-State Physics, Center for Hybrid Nanostructures, Luruper Chaussee 149, 22761 Hamburg, Germany

[2] The Hamburg Center for Ultrafast Imaging, 22761 Hamburg, Germany

[3] University of Hamburg, Department of Chemistry, HARBOR, Luruper Chaussee 149, 22761 Hamburg, Germany

[4] Deutsches Elektronen-Synchrotron DESY, Notkestraße 85, 22607 Hamburg, Germany

[5] University of Hamburg, Department of Chemistry, Grindelallee 117, 20146 Hamburg, Germany

[6] ESRF, The European Synchrotron, 71 Avenue des Martyrs, CS40220, 38043 Grenoble Cedex 9, France

Abstract:

The key to control the fabrication process of transition metal sulfide nanocrystals is to understand the reaction mechanism, especially the coordination of ligands and solvents during their synthesis. We utilize *in situ* High-Energy Resolution Fluorescence Detected X-ray Absorption Spectroscopy (HERFD-XAS) as well as *in situ* valence-to-core X-ray Emission Spectroscopy (vtc-XES) combined with Density Functional Theory (DFT) calculations to identify the formation of an octahedral $[Zn(OA)_6]^{2+}$ complex, and the ligand exchange to a tetrahedral $[Zn(SOA)_4]^{2+}$ complex (OA = oleylamine, OAS = oleylthioamide), during the synthesis of ZnS nanorods in oleylamine. We observe *in situ* the transition of the electronic structure of $[Zn(SOA)_4]^{2+}$ with a HOMO/LUMO gap of 5.0 eV towards an electronic band gap of 4.3 eV and 3.8 eV for 1.9 nm large ZnS wurtzite nanospheres and 2 x 7 nm sphalerite nanorods, respectively. Thus, we demonstrate how *in situ* multimodal X-ray spectroscopy and scattering studies can not only resolve structure, size, and shape during the growth and synthesis of NPs in organic solvents and at high temperature but also give direct information about their electronic structure, which is not readily accessible through other techniques.

Introduction:

Zinc sulfide (ZnS) plays an important role in a wide range of applications, such as optoelectronic devices and field emitters,[1] photodetectors,[2] photocatalysis,[3-5] and protective shell material in core-shell nanostructures.[6, 7] Particularly, anisotropic structures like nanorods or nanosheets are of great interest, due to charge carrier confinement in different dimensions.[8] ZnS exhibits two crystal structures, sphalerite or zinc blende (cubic) and wurtzite (hexagonal) phases.[9] The phase transition from sphalerite to wurtzite can be either induced by thermal annealing at temperatures above 1000 °C [10-12] or directly in the solvothermal synthesis of nanocrystals (NC) at temperatures around 150 °C.[13-17]

Among non-aqueous synthesis routes,[17-21] the combination of elemental sulfur and oleylamine is widely explored in the synthesis of transition metal sulfides,[18] particularly of ZnS,[19, 22] but the understanding of their reaction with the metal precursor is still under debate.[21] It has been reported that elemental sulfur and oleylamine form various polysulfides under the formation of H_2S,[18, 23] but so far it is not clear which polysulfide species interacts with the metal precursor and actively takes part in the formation of transition metal sulfides. The interaction between zinc acetate ($Zn(Ac)_2$) and elemental sulfur in oleylamine has not been studied to date *in situ*.

Optical methods like visible light fluorescence and absorption, commonly used for studying the semiconducting QDs, can hardly be utilized to follow *in situ* changes of the electronic structure of Zn species in solution due to the large ZnS band gap that overlaps with the absorption of the organic ligands in the reaction solution.[24] X-ray Absorption Spectroscopy (XAS),[25, 26] particularly High-Energy Resolution Fluorescence Detected X-ray Absorption Spectroscopy (HERFD-XAS), is element-specific and offers sensitivity to the local environment around the absorbing atom.[27-29,30] Data acquisition for HERFD-XAS is challenging due to the need to balance data quality, time resolution, and X-ray radiation damage. Additionally, valence-to-core X-ray Emission Spectroscopy (vtc-XES) enables to probe the valence orbitals and can provide detailed information e.g. about ligand bonds to a metal center by mapping the occupied molecular orbitals.[31-33] The vtc-XES signal at the Zn edge is over 100 times weaker than core-to-core XES transitions, necessitating extended data acquisition times.[34-36]

Combining HERFD-XAS with X-ray scattering provides a comprehensive overview of the reaction pathways across various length scales,[36-38] by revealing a wide range of structural,

chemical, and electronic properties of materials.[39-44] However, there are no combined *in situ* HERFD-XAS/vtc-XES studies on the nucleation and growth of nanoparticles at high temperatures in solution at relevant time scales.

In this work, we conduct *in situ* experiments at a fourth-generation synchrotron, which provides enhanced flux and thus enables faster acquisition of vtc-XES data. We present a methodology to elucidate the chemical pathways leading to the formation of ZnS NC in the oleylamine-sulfur system, together with the emergence of their electronic properties by complementary *in situ* HERFD-XAS, vtc-XES, PXRD, and SAXS. Thereby, we prove the formation of a $[Zn(OA)_6]^{2+}$ and $[Zn(SOA)_4]^{2+}$ complex (OA = oleylamine, SOA = oleylthioamide) and track their reaction to ZnS NC in wurtzite phase (w-ZnS) and the transition to ZnS nanorods in sphalerite phase (s-ZnS).

Results & Discussion

Chemical transformation of $Zn(Ac)_2$ and elemental sulfur in oleylamine

We first investigate the coordination of Zn^{2+} ions at room temperature after the dissolution of $Zn(Ac)_2$ in oleylamine, before and after the addition of elemental sulfur. To unveil the nature of the Zn complexes formed, we compare the HERFD-XAS and vtc-XES measurements with the theoretical spectra simulated by ORCA DFT, as shown in **Figure 1**. The spectrum of $Zn(Ac)_2$ dissolved in oleylamine exhibits a 0.8 eV shift in the XAS whiteline (ca. 9.665 keV) to lower energies and a 0.6 eV shift of the $K\beta_{2,5}$ peak (ca. 9.657 keV) to higher energies, compared to the $Zn(Ac)_2$ reference, while the intensity of the whiteline increased. The energy shifts might suggest the replacement of the Zn-O coordination by Zn-N coordination while the increased whiteline intensity indicates a change in the coordination of the Zn atom, from tetrahedral to octahedral. By comparing the experimental and simulated spectra, we prove that the dissolution of $Zn(Ac)_2$ in oleylamine leads to the displacement of the acetate ligands by six oleylamine molecules, resulting in an octahedral $[Zn(OA)_6]^{2+}$ complex, visualized in **Figure 1b.** The DFT calculations show that only the octahedral N-coordinated complex matches the experimental data as shown in **Figure 1b**, **Figure SI1a,** and **Figure SI2.**

The addition of elemental sulfur leads to a 0.6 eV shift of the whiteline to lower energies, while the $K\beta_{2,5}$ peak shifts 0.6 eV to higher energies, compared to the mixture without sulfur, as shown in **Figure 1c.** Furthermore, the addition of sulfur also results in a decrease in whiteline intensity. The energy shifts result from a ligand exchange around Zn, where the Zn-N coordination is replaced by Zn-S. The decrease in whiteline intensity indicates that the coordination number of Zn decreased from six to four. The theoretical XAS and XES spectra obtained from DFT (blue dashed line) simulations reveal that six oleylamine chains of the $[Zn(OA)_6]^{2+}$ complex are replaced by four of their corresponding thioamide derivatives, resulting in the $[Zn(SOA)_4]^{2+}$ complex shown in **Figure 1a.** The formation of other Zn-S coordination, like $[Zn(H_2S)_4]^{2+}$ is ruled out in **Figure SI1b**.

The change from an octahedral to a tetrahedral coordination geometry might be related to the steric hindrance of sulfur atoms, which occupy more space compared to nitrogen. Additional information on the formation of the tetrahedral $[Zn(SOA)_4]^{2+}$ complex is reported in **Figure SI3**. To match the absolute energy scale of the theoretical and experimental spectra, the calculated energy positions were corrected, as described in **Figure SI2.**

Thus, our experiments demonstrate that oleylamine and sulfur react already at room temperature in the presence of Zn^{2+} ions, forming the thioamide derivative of oleylamine, which so far has been evidenced by NMR and SAXS only at elevated reaction temperatures.[18, 23] ^{13}C NMR spectroscopy shows evidence of the thioamide functional group only in mixtures of oleylamine and sulfur heated at temperatures above 170 °C (see **Figure SI4-5** and supplementary notes).

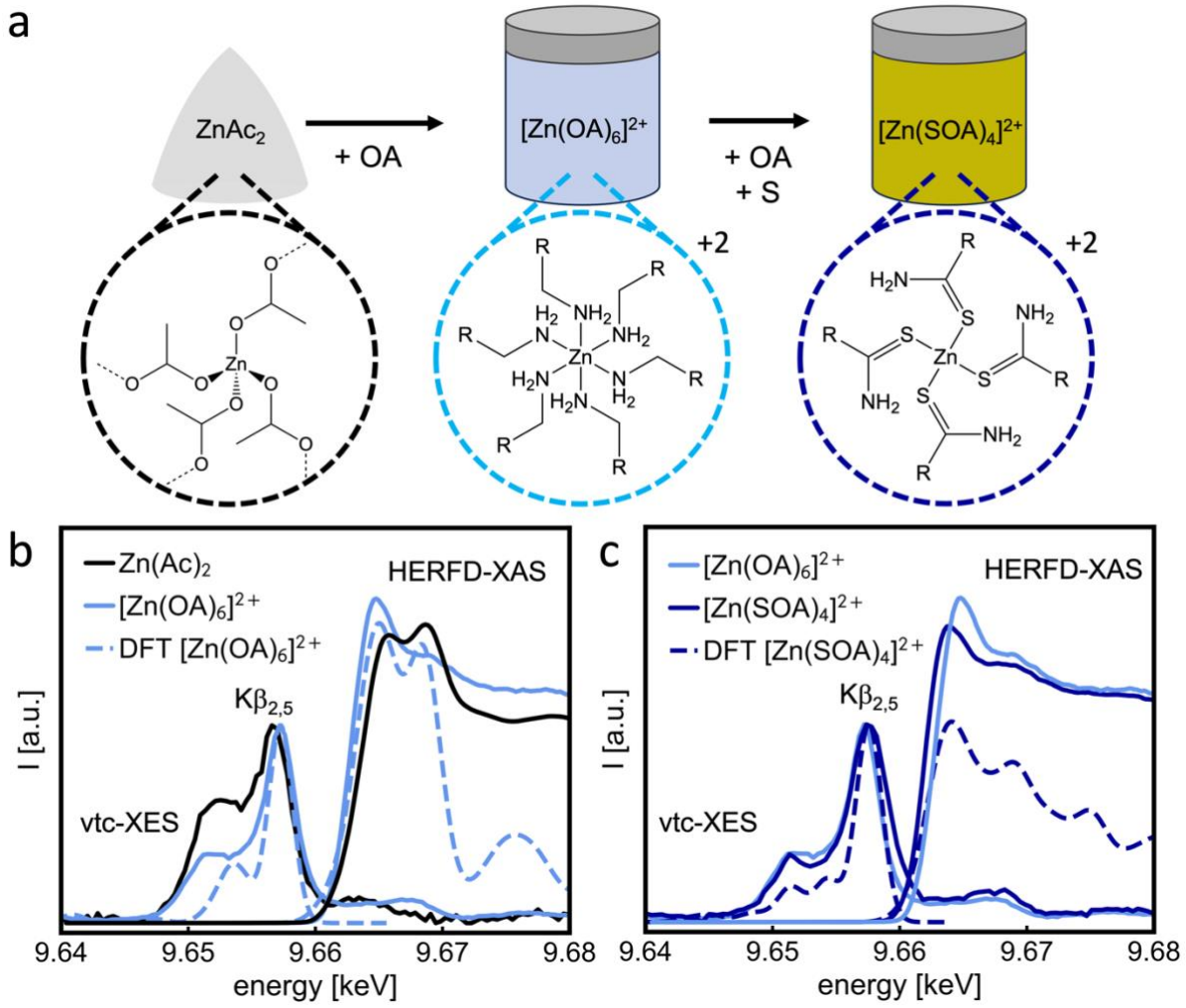

Figure 1: Identifying Zn coordination by HERFD-XAS analysis (a) Schematics of the reaction pathway from $Zn(Ac)_2$ precursor (black dashed circle) to a tetrahedral $[Zn(SOA)_4]^{2+}$ complex, (dark blue), which undergoes an intermediate step: an octahedral $[Zn(OA)_6]^{2+}$ complex (light blue). The six oleylamine chains are replaced by four of their corresponding thioamide derivatives upon adding sulfur to the mixture. **(b)** Comparison of experimental HERFD-XAS spectra of $Zn(Ac)_2$ (black line) and $Zn(Ac)_2$ dissolved in oleylamine (light blue solid line) with the theoretical spectra obtained using DFT calculations of the proposed $[Zn(OA)_6]^{2+}$ complex (light blue dashed line). **(c)** Experimental spectra of $Zn(Ac)_2$ dissolved in

oleylamine with and without elemental sulfur, forming $[Zn(OA)_6]^{2+}$ and $[Zn(SOA)_4]^{2+}$ complexes, respectively. (R = $(CH_2)_7(HC{=}CH)(CH_2)_7(CH_3)$).

In situ HERFD-XAS and vtc-XES resolving the electronic structures during the synthesis

In **Figure 2a**, we present the *in situ* vtc-XES and HERFD-XAS datasets, which track the reaction of $[Zn(SOA)_4]^{2+}$ to s-ZnS NC (s = sphalerite). The HERFD-XAS data reveals a splitting of the whiteline during the formation of s-ZnS, as highlighted in the inset with peaks A and B. While the evolving shoulder (A) shifts to lower energy, which is typical for ZnS, the absorption maximum (B) shifts to higher energies.[29, 45] Notably, the intensity of the whiteline remains almost constant during the reaction which indicates a constant tetrahedral coordination of the Zn atoms through the reaction. The broadening of peaks B and C results in a non-global minima between the peaks which is untypical for s-ZnS and might suggest the co-formation of w-ZnS (W = wurtzite). To analyze the fraction of w-ZnS in the final product, MCR-ALS analysis was performed.[46, 47] Further information about the MCR-ALS method is available in the **SI, Figure SI6, Table SI1-2**.

The MCR-ALS analysis allows us to track the time and temperature-dependent concentration profile of all components in the reaction, as shown in **Figure 2b**. In total, three different components are present during the reaction. In addition to the $[Zn(SOA)_4]^{2+}$ starting complex and the s-ZnS, w-ZnS are identified as a by-product of the reaction. The recovered spectra of these components are shown in **Figure 2b top**, while their concentration profile is shown in **Figure 2b bottom**. At 40 °C, the $[Zn(SOA)_4]^{2+}$ complex begins to convert to w-ZnS. Upon reaching 110 °C, the transformation of the $[Zn(SOA)_4]^{2+}$ complex into w-ZnS is completed, marking the onset of the formation of s-ZnS. As the reaction temperature reaches 155 °C, the formation of s-ZnS persists, resulting in a final product composition of 60% w-ZnS and 40% s-ZnS.

Beyond the component analysis with MCR-ALS analysis, we combined *in situ* HERFD-XAS with *in situ* vtc-XES data to monitor the HOMO/LUMO gap during the reaction. For this, we calculated the energy difference between the resonant excitation in HERFD-XAS (1s => 4p - LUMO) and the highest energetic recombination in vtc-XES (3p => 1s - HOMO). The total energy scheme for photon-in (Ω) and photon-out (ω) spectroscopy with ground, intermediate, and final states at the Zn edge is shown in **Figure 2c**. The HOMO/LUMO gap was calculated by the difference between the global minima of the first derivative of the vtc-XES and the global maxima of the first derivative of the HERFD-XAS, as described in **Figure 2d.** More detailed information regarding the *in situ* HOMO/LUMO gap determination is available in SI.

We observe a decrease in the HOMO/LUMO gap (ΔE) as the reaction progresses and the transformation of the $[Zn(SOA)_4]^{2+}$ complex to the w-ZnS and s-ZnS takes place (**Figure 2e**). To calibrate the energy scale, we set the E at the end of the reaction to the band gap of s-ZnS (3.8 eV). We determine the HOMO/LUMO gap of the $[Zn(SOA)_4]^{2+}$ complex to be 5.0 eV. At 155 °C reaction temperature and a ramping rate of 1 °C/min, the HOMO/LUMO gap changes stepwise. First ΔE quickly drops by 0.7 eV from 5.0 eV to 4.3 eV, which reflects the band gap of w-ZnS during our synthesis. Therefore, we assume that the band structure has already evolved after 40 minutes. The band gap is comparably high for w-ZnS, which suggests a very small crystallite size due to quantum confinement effects.[48] To estimate the size of the w-ZnS we have performed atomic effective pseudopotential calculations followed by configuration interaction and obtained, for an electronic gap of 4.3 eV a diameter of around 1.8 nm, as described in **Figure SI7**.[49-55] After 100 minutes, the value reached 3.8 eV, which coincidences with the onset of s-ZnS formation shown in **Figure 2b**.

Moreover, the band gap ΔE estimation is consistent with the values determined by using *ex situ* UV-vis of unwashed aliquots (**Figure 2e, Figure SI8, and Table SI3**). UV-Vis analysis struggles to discriminate between organic background and emerging w-ZnS, which explains the discrepancy, especially at the early reaction state.

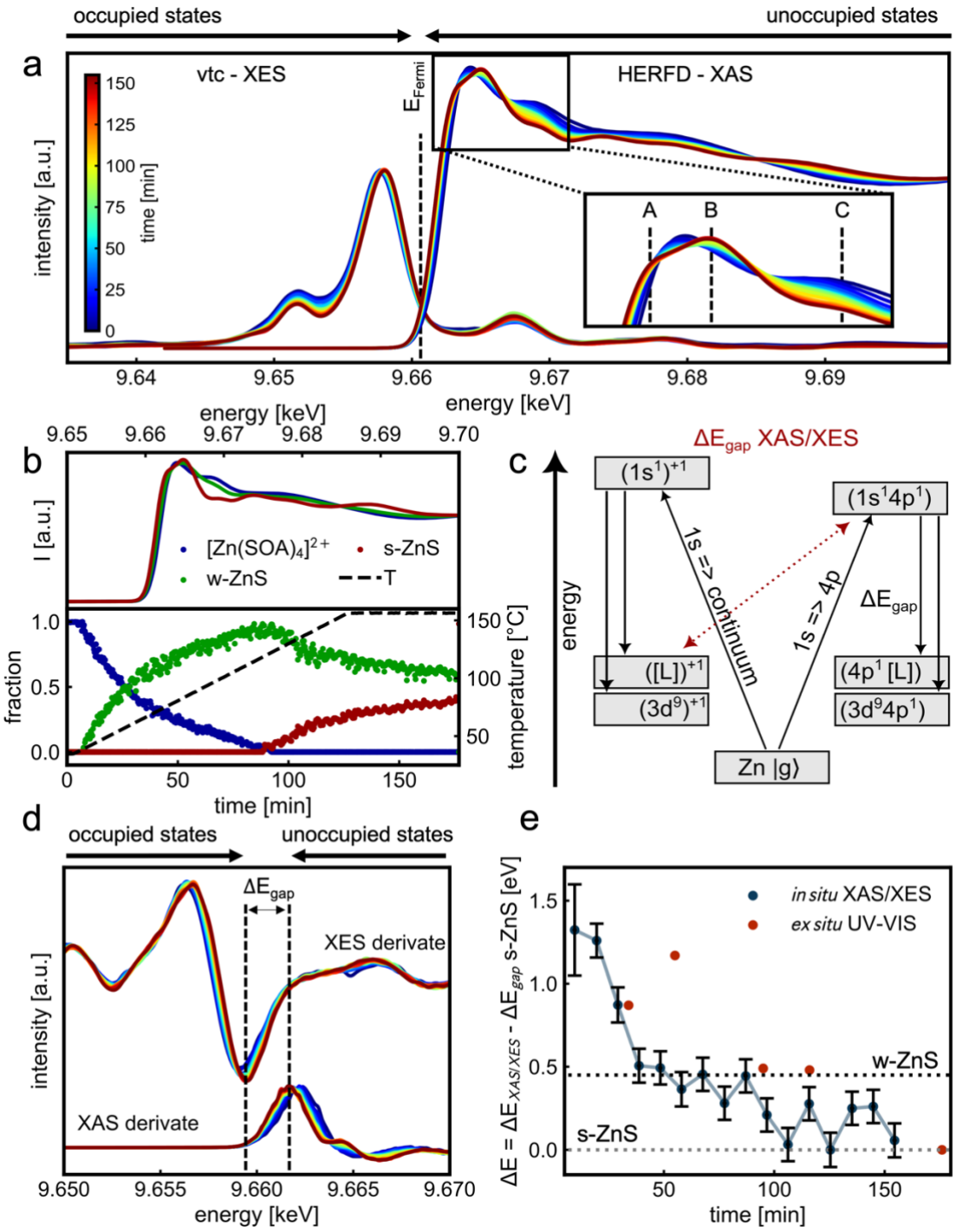

Figure 2: *In situ* X-ray spectroscopy of the synthesis of s-ZnS. (a) *In situ* Zn K-edge vtc-XES and HERFD-XAS spectra of the synthesis of s-ZnS where changes in the XAS are highlighted in the inlet. **(b)** MCR-ALS analysis of *in situ* HERFD-XAS data reveals individual contributions of three independent compounds, the $[Zn(SOA)_4]^{2+}$ complex, w-ZnS, and s-ZnS. **(c)** Schematic interstate transitions during non-resonant (left) and resonant (right) excitation result in a difference in the calculated band gap. **(d)** The difference between the minimum of the derivation of the XES signal and the maximum of the derivation of the XAS signal reflects the HOMO/LUMO gap during the preparation of s-ZnS. **(e)** The HOMO/LUMO gap values

determined by *in situ* XAS/XES during the reaction in solution are compared with the HOMO/LUMO optical gap values determined with *ex situ* UV-VIS analysis of unwashed aliquots (red).

Simultaneous *in situ* SAXS and PXRD resolving the atomic structures during the synthesis

To characterize the structural evolution of w-ZnS and s-ZnS, *in situ* small-angle X-ray scattering (SAXS) and powder X-ray diffraction (PXRD) was performed and compared with *ex situ* High-Resolution Transmission Electron Microscopy (HRTEM) images. The *in situ* SAXS data (**Figure 3a**) show an increased intensity at low q starting at approximately 70 minutes, indicating particle formation during the reaction. The particle size was calculated by applying a spherical fitting model to the experimental data, with the results shown in **Figure 3d**. The energy of >100 keV and the resulting high q-min of around 0.1 $Å^{-1}$ restricted the resolution to structures larger than 8 nm. However, the high background (lamellar, solvent) prevented us from deconvoluting the data into distinct spherical fits for w-ZnS and rod-like fits for s-ZnS. Further details about the SAXS fitting and background subtraction are available in **Figure SI9-12**. Furthermore, the formation and dissolution of oleylamine lamellar structures were observed in the presence of zinc ions in solution, as depicted in **Figure SI10**, aligning with findings from related studies on synthesis under similar reaction conditions.[23]

In situ PXRD data corroborate the previously described transformation of w-ZnS to s-ZnS during the reaction. This trend is evident by comparing the intensity ratios between the reflections of w(113) and s(220)/w(210), as depicted in **Figure 3a**. At around 110 minutes, the intensities of both reflections are equal. Thereafter, the intensity ratio shifts towards s(220)/w(210) until the reaction concludes. Additionally, PXRD data reveal a strong preferred orientation along the s(111) axis. The formation of spherical w-ZnS as an intermediate in the formation of s-ZnS nanorods is already observed in comparable systems,[15] where the preferred orientation is explained by an oriented attachment of w-ZnS.[14]

This preferred orientation in s-ZnS is also evidenced by HRTEM analysis of aliquots taken throughout the reaction, as shown in **Figure 3b**. At 75 minutes, the formation of w-ZnS results in spherical NC with an estimated size of 1.9 ± 0.2 nm, which is in agreement with 1.8 nm obtained by HERFD-XAS/vtc-XES. Detailed size analysis and full images are provided in **Figure SI13-15**.

While MCR-ALS analysis proposes that the formation of w-ZnS starts at 40 °C, SAXS and PXRD and HRTEM analysis confirm only the formation above 90 °C. This mismatch can be explained by the varying sensitivity of all methods. X-ray spectroscopy can detect already non-crystalline species and even molecular complexes, while SAXS and PXRD are highly sensitive to the crystal structure and shape of ZnS NC.

The preferred orientation, as well as the fractions of w-ZnS and s-ZnS, can be extracted from the PXRD data through sequential Rietveld refinement, as illustrated for the final PXRD pattern in **Figure 3c.** The Rietveld analysis fits a spherical model to the w-ZnS with a domain size of approximately 2 nm, while the s-ZnS demonstrates a preferred orientation along s(111) and a domain 2 nm x 7 nm. The fraction and domain sizes of s-ZnS and w-ZnS change throughout the reaction, as shown in **Figure 3d** and **Figure SI16**. To compare the domain sizes calculated from the PXRD data with those obtained from the SAXS fit, the PXRD sizes were averaged, considering the varying phase fractions at different time points. The PXRD sizes are systematically underestimated compared to the SAXS sizes, as they reflect the domain size, whereas SAXS fitting represents the solvation size of nanoparticles in the solution. The ratio between s-ZnS and w-ZnS can be changed by increasing the reaction temperature to 170°C and the ramping rate to 10°C/min, as discussed in **Figure SI17**.

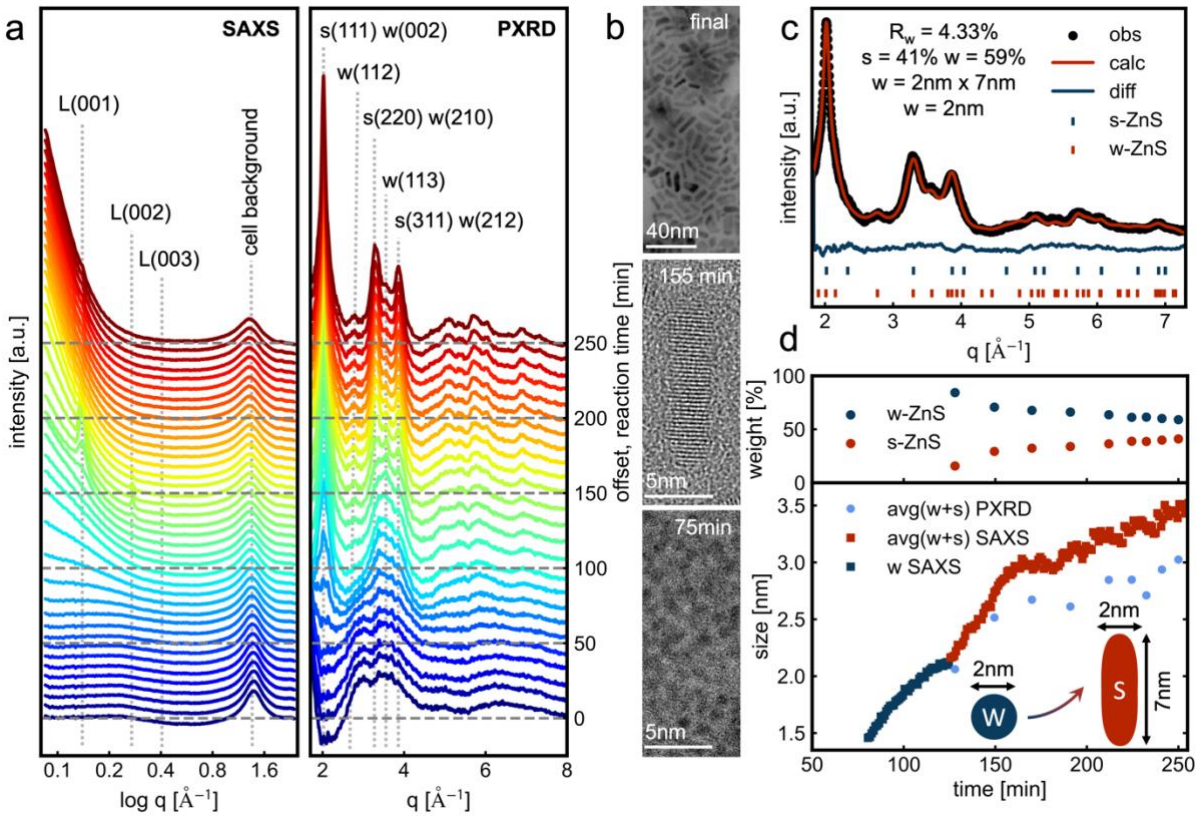

Figure 3: Simultaneous *in situ* SAXS and PXRD, as well as *ex situ* HRTEM analysis. **(a left)** *In situ* SAXS analysis shows an increasing intensity at low q, starting after approximately 70 minutes of reaction, indicating the formation of spherical nanoparticles. The oleylamine lamellae (L) and cell background (≈ 1.5 $Å^{-1}$) were indicated at the top. **(a right)** *In situ* PXRD analysis shows the formation of w-ZnS reflections after 70 minutes, with changes in the relative intensity of the w(210)/s(220) and w(113) peaks over time, revealing the formation of the s-ZnS phase during the reaction. The s(111) peak have comparable high intensity, thus implying a preferred orientation in the s-ZnS along the s(111) facet. **(b)** HRTEM analysis of washed aliquots of the reaction reveals the formation of ZnS nanorods after 120 minutes, which explains the preferred orientation along s(111), while at 75 minutes only spherical particles with 1.9 ± 0.2 nm are observed. **(c)** Rietveld analysis of the final product shows the presence of 41% s-ZnS and 59% w-ZnS. Moreover, the Rietveld analysis refines a spherical domain size of 2 nm in the w-ZnS and anisotropic domain sizes of 2 nm x 7 nm in the s-ZnS. The fraction of s-ZnS to w-ZnS evolves throughout the reaction, as shown in the top panel of **(d)**. The size calculated by fitting the SAXS data with a spherical model is compared with the average size obtained from the Rietveld analysis in the bottom panel of **(d)**.

Conclusion:

This work extends the application of Zn K-edge XAS and vtc-XES in inorganic and bioinorganic chemistry to investigate the emergence and growth of nanomaterials in solution at high temperatures. The integration of HERFD-XAS, $K\beta_{2,5}$ XES, and DFT theory allows for the identification of successive Zn-O, Zn-N, and Zn-S ligand exchanges.

Our findings reveal that even at room temperature, $Zn(Ac)_2$ undergoes a reaction with oleylamine to form an octahedral $[Zn(OA)_6]^{2+}$ complex, which, upon sulfur addition, transforms into a tetrahedral $[Zn(SOA)_4]^{2+}$ complex. This rules out the formation of e.g. hydrogen sulfide Zn complexes, such as $[Zn(H_2S)_4]^{2+}$. By tracking the *in situ* heating of the $[Zn(SOA)_4]^{2+}$ complex above 155 °C, we observe the successive nucleation and growth of sphalerite and wurtzite ZnS nanostructures. Interestingly, we also monitor the evolution of the HOMO/LUMO gap from 5.0 to 4.3 and eventually to 3.8 eV, consistent with the $[Zn(SOA)_4]^{2+}$ complex and the 1.8 nm wurtzite and sphalerite structures, respectively.

The structural transformation of ZnS was further analyzed through simultaneous *in situ* SAXS and PXRD measurements. Our observations capture the formation of wurtzite spherical ZnS particles, progressing to the transformation into sphalerite ZnS rods oriented predominantly along the (111) axis. The shape, size, and band gap energy of the nanoparticles were validated through *ex-situ* HRTEM and UV-vis spectroscopy of powder samples.

In conclusion, this study provides a detailed insight into the coordination chemistry and structural changes during the synthesis of ZnS nanocrystals. The methodology showcases its potential to monitor the structural and electronic transitions during particle growth at elevated temperatures, particularly in scenarios where optical spectroscopy is not feasible. This approach holds promise for the study of other materials with high energy band gaps or in reaction environments where optical spectroscopy is limited, and elemental specificity is crucial for analysis in the future.

Acknowledgement:

This research was supported by the European Research Council (LINCHPIN project, grant no. 818941), the Deutsche Forschungsgemeinschaft (DFG) through the Cluster of Excellence "Advanced Imaging of Matter" (EXC 2056, project ID 390715994) and the Graduate School "Nanohybrid" (funding ID 408076438), and the Bundesministerium für Bildung und Forschung (BMBF) via the project 05K22GU7 (LUCENT II). Furthermore, we acknowledge DESY (Hamburg, Germany), a member of the Helmholtz Association, for the provision of experimental facilities. Parts of this research were carried out at PETRA III using beamlines P07 and P21.1 and P62 and at ESRF using beamline ID26 under proposals MA5353, MA5366 and HC-4929. [56-58]

Methods:

Chemicals:

Zinc (II) acetate ($Zn(Ac)_2$) (99.99%, anhydrous), sulfur (99.998% trace metal basis), and oleylamine (≥98% primary amine) were purchased from Sigma-Aldrich. All chemicals were used as received without further purification and stored, except for the sulfur, under an argon atmosphere.

Synthesis of ZnS:

The ZnS synthesis was performed in the *in situ* cell adopted from previous work[36, 59, 60], as described in **Figure SI18**. Two individual solutions were prepared in oleylamine. First, 0.0489 g of $Zn(Ac)_2$ powder was dissolved in 1 mL of oleylamine. Then, 0.0128 g of sulfur was dissolved in 2 mL of oleylamine. Both solutions were stirred for one hour at room temperature under an argon atmosphere. The solutions were added into the microreactor in a volume ratio of 2:1 elemental sulfur:$Zn(Ac)_2$ solutions in a total volume of 66 µL and 174 µL for the scattering and spectroscopic experiments, respectively. The reactor was sealed under argon 6.0 and heated at a heating rate of 1 °C/min to 155 °C or at a heating rate of 10 °C/min to 170 °C. The *ex situ* samples for UV-Vis analysis were prepared under the same conditions in the *in situ* spectroscopy cell.

UV-Vis: UV-visible spectra were collected using the Cary 60 UV-VIS spectrometer (Agilent Technologies Inc., US) and a quartz cuvette. The samples were diluted with cyclohexane in the cuvette. The HOMO/LUMO gap and the band gap were calculated using the Tauc-Plot.[61]

NMR: Nuclear magnetic resonance (NMR) spectra were recorded on a Bruker Avance NEO 600 MHz NMR spectrometer using TopSpin 4.1.3 (BRUKER BIOSPIN GmbH, Rheinstetten, Germany) equipped with a 5 mm TCI Cryoprobe cooled with liquid nitrogen, operating at 600.25 MHz and 298.0 K. All chemical shifts were referenced to residual solvent peaks [$CDCl_3$: 7.26 ppm (^1H), 77.2 ppm (^{13}C); C_6D_6: 7.3 ppm (^1H), 128.0 ppm (^{13}C)]. One-dimensional (1D) ^1H and two-dimensional (2D) (^1H,^{13}C)-HSQC and 2D (^1H,^{13}C)-HMBC spectra were acquired using standard pulse sequences from the Bruker library. For the 1D

$^{13}C\{^{1}H\}$-NMR spectra (zgpg30) of the reaction mixture at room temperature, 1024 and 10240 scans (NS) were recorded.

Sample preparation for NMR analysis:

Sulfur in oleylamine: Under ambient conditions, sulfur powder (9.1 mmol) was introduced in a glass vial with further addition of oleylamine (45.5 mmol). The solution was stirred at room temperature until all sulfur was dissolved. The reaction mixture was heated to 170 °C by using an oil bath with stirring, and aliquots were taken at 60, 100, and 140 °C. When the solution reached 170 °C, the temperature was kept for 20 min, and the corresponding aliquot was taken. The mixture was further heated to 190 °C and was kept at 200 °C for 40 minutes before collection of the 200 °C aliquot.

$Zn(Ac)_2$ and S in oleylamine: Under ambient conditions, $Zn(Ac)_2$ (6.65 mmol) was introduced in a glass vial with further addition of oleylamine (45.5 mmol). The solution was stirred at room temperature for 30 min and sulfur (9.1 mmol) was added to the mixture as one portion followed by a further 50 min of stirring.

STEM and HRTEM analysis: STEM images were taken and probe-corrected with a Regulus 8220 (Hitachi High Technologies Corp., Japan) at an acceleration voltage of 30 kV and using the BFSTEM acquisition mode. HRTEM images were taken with a JEOL JEM-2200FS (JEOL Ltd., Japan) using an acceleration voltage of 200 kV.

Beamline setup and data acquisition:

The *in situ* HERFD-XAS and vtc-XES spectra were recorded at the ID26 beamline at the European Synchrotron Radiation Facility (ESRF), Grenoble, France. The HERFD-XAS were collected by measuring the intensity of the Zn K_a main line using a Si(642) crystal in Rowland Geometry while scanning the incident energy. The position of the X-ray beam was moved on the reaction cell to minimize radiation damage. XAS spectra were acquired every 16 s with an energy range from 9.64 to 9.8 keV and a stepsize of 0.2 eV. The vtc-XES spectra were recorded using four Ge(555) crystals in Rowland geometry over a total energy range from 9.63 to 9.71 keV. To decrease the acquisition time, the spectra region from 9.63 to 9.69 keV was measured with energy steps of 0.4 eV and an acquisition time of 532s (with motor movements),

while the range from 9.69 to 9.71 keV was recorded in steps of 2 eV with a total acquisition time of 44 s.

The X-ray total scattering and SAXS *in situ* data were collected in a SAXS/WAXS combined setup at the second experimental hutch (EH2) at beamline P07 of PETRA III at Deutsches Elektronen-Synchrotron (DESY), Hamburg, Germany.[62] The total scattering and SAXS data were collected every 0.5 s using two flat panel detectors (Varex XRD4343CT, Varex Imaging Corp., USA) with 2880 x 2880 pixels of 150 x 150 μm^2 size. During the experiments to synthesize W and S ZnS at 155 °C, the sample-to-detector distances (SDD) were 0.812 m for total scattering and 4.636 m for the SAXS data, determined from the calibration with LaB_6 calibrant, at an X-ray beam energy of 103.56 keV. For the synthesis at 170 °C with 10 °C/min heating rate, the SDD was determined as 0.765 m for total scattering data collection, obtained from calibration with LaB_6, and 4.613 m for the SAXS, from CeO_2 calibrant, at an X-ray beam energy of 103.60 keV.

The *ex situ* total scattering data were taken at Beamline P21.1 at PETRA III, DESY.[S2] The total scattering data were recorded with a Varex flat panel detector model XRD4343CT at an SDD of 0.377 m. Samples were enclosed in a quartz capillary, and the calibration was carried out by measuring the LaB_6 calibrant at an X-ray beam energy of 101.60 keV.

The *ex situ* SAXS data shown in Figure SI9 are collected at Beamline P62 at PETRA III, DESY.[63] The energy was set to 12 keV using a Si(111) monochromator. The beam size was 0.5x0.5 mm^2. The samples were mounted vertically in a multi-capillary holder. The sample-to-detector distances were calibrated to be 2.849 m using AgBH. The SAXS signals were collected by Eiger2 9M detector.

Data processing:

The HERFD-XAS and the vtc-XES data were processed using a self-written Python code. The vtc-XES data were normalized by the maximum intensity. The determination of the XAS edge position and normalization of the edge jump were performed by using the LARCH-XAFS module.[64] The spectroscopic data were treated with a Savitzky-Golay filter and further processed with the NumPy and SciPy package.[65, 66] The processed data are compared with raw data in Figure SI18. The simulations of the XAS spectra were carried out using the ORCA 5.0.4 code[67], where the initial zinc complexes for DFT optimization were built using Avogadro: an

open-source molecular builder and visualization tool. Version 1.2.0. [68] The Orca input files were adapted from *Stepanic et.al.*[25]

Azimuthal integration of the 2D detector patterns for PXRD and SAXS data was performed with the Python module pyFAI after masking out beam stop shadows, glitches, pixel defects, and noisy pixels.[69] For the background subtraction, *in situ* total scattering data of sulfur dissolved in oleylamine and pure oleylamine were collected under the same reaction conditions of the ZnS syntheses at 155 and 170°C, respectively. The background was subtracted from the original data set. The data were averaged over 60 frames, corresponding to 30 s time resolution. The Rietveld refinement was performed with GSAS-II package[70], employing a two-phase refinement with ZnS sphalerite and wurtzite phases sharing one particle size parameter. The sphalerite phase (ICSD-230703) and wurtzite phase (ICSD-67453) were taken from the ICSD database. The refinement was carried out in a sequential way starting from the XRD at the end of the reaction and going backward to earlier reaction times, ensuring a better reliability of the fit.

The fitting of the SAXS data was carried out over the range of 0.08 to 1.8 $Å^{-1}$. An empty capillary background was measured at room temperature and subtracted from the original *in situ* SAXS data set. The SAXS data were averaged over 120 frames (1 min resolution) and 10 frames (5 s resolution) for the ZnS reactions at 155 °C and 170 °C, respectively. The fit was carried out in SASview 5.0.6 [71] with the DREAM algorithm.[72] As a fitting function, a plugin was used, which contained a power law, a sphere, a symmetric pseudo-Voigt profile and a fitting function for the lamellae. The lamellae were fitted with a triplet of asymmetric pseudo-Voigt profiles sharing the ratio of Gauss to Lorentz factor eta and the FWHM. The peak height ratio was kept constant, while q was allowed a relaxation of ± 5% of the multiple of the first peak. For the reaction temperature of 170 °C, an additional sphere model was used with a constant radius of 5.11 Å, and to match the background, the first peak of the lamellae was constrained to be a Lorentz profile only, while the second and third peak shared the ratio of Gauss to Lorentz factor eta.

To improve the grammar and wording in parts of the manuscript and supporting information, ChatGPT 4 omni was used for proofreading, following the guidelines for using AI in scientific publications.[73]

References

(1) Chen, Z.-G.; Cheng, L.; Xu, H.-Y.; Liu, J.-Z.; Zou, J.; Sekiguchi, T.; Lu, G. Q.; Cheng, H.-M. ZnS Branched Architectures as Optoelectronic Devices and Field Emitters. *Advanced Materials* **2010**, *22* (21), 2376-2380. DOI: 10.1002/adma.200903643.

(2) Zeng, X.; Pramana, S. S.; Batabyal, S. K.; Mhaisalkar, S. G.; Chen, X.; Jinesh, K. B. Low temperature synthesis of wurtzite zinc sulfide (ZnS) thin films by chemical spray pyrolysis. *Physical Chemistry Chemical Physics* **2013**, *15* (18), 6763-6768, 10.1039/C3CP43470B. DOI: 10.1039/C3CP43470B.

(3) Lange, T.; Reichenberger, S.; Ristig, S.; Rohe, M.; Strunk, J.; Barcikowski, S.; Schlögl, R. Zinc sulfide for photocatalysis: White angel or black sheep? *Progress in Materials Science* **2022**, *124*, 100865. DOI: 10.1016/j.pmatsci.2021.100865.

(4) Hao, X.; Wang, Y.; Zhou, J.; Cui, Z.; Wang, Y.; Zou, Z. Zinc vacancy-promoted photocatalytic activity and photostability of ZnS for efficient visible-light-driven hydrogen evolution. *Applied Catalysis B: Environmental* **2018**, *221*, 302-311. DOI: 10.1016/j.apcatb.2017.09.006.

(5) Mróz, K.; Kobielusz, M.; Orzeł, Ł.; Macyk, W. Spectroscopic and Spectroelectrochemical Studies on Redox Properties of Zinc Sulfide and Their Consequences on Photocatalytic Activity. *The Journal of Physical Chemistry C* **2023**, *127* (35), 17366-17376. DOI: 10.1021/acs.jpcc.3c04298.

(6) Boercker, J. E.; Woodall, D. L.; Cunningham, P. D.; Placencia, D.; Ellis, C. T.; Stewart, M. H.; Brintlinger, T. H.; Stroud, R. M.; Tischler, J. G. Synthesis and Characterization of PbS/ZnS Core/Shell Nanocrystals. *Chemistry of Materials* **2018**, *30* (12), 4112-4123. DOI: 10.1021/acs.chemmater.8b01421.

(7) Ji, B.; Koley, S.; Slobodkin, I.; Remennik, S.; Banin, U. ZnSe/ZnS Core/Shell Quantum Dots with Superior Optical Properties through Thermodynamic Shell Growth. *Nano Letters* **2020**, *20* (4), 2387-2395. DOI: 10.1021/acs.nanolett.9b05020.

(8) Fang, X.; Wu, L.; Hu, L. ZnS Nanostructure Arrays: A Developing Material Star. *Advanced Materials* **2011**, *23* (5), 585-598. DOI: 10.1002/adma.201003624.

(9) Rajaitha, P. M.; Hajra, S.; Sahu, M.; Mistewicz, K.; Toroń, B.; Abolhassani, R.; Panda, S.; Mishra, Y. K.; Kim, H. J. Unraveling highly efficient nanomaterial photocatalyst for pollutant removal: a comprehensive review and future progress. *Materials Today Chemistry* **2022**, *23*, 100692. DOI: 10.1016/j.mtchem.2021.100692.

(10) Scott, S. D.; Barnes, H. L. Sphalerite-wurtzite equilibria and stoichiometry. *Geochimica et Cosmochimica Acta* **1972**, *36* (11), 1275-1295. DOI: 10.1016/0016-7037(72)90049-X.

(11) Li, Y.; Tan, W.; Wu, Y. Phase transition between sphalerite and wurtzite in ZnS optical ceramic materials. *Journal of the European Ceramic Society* **2020**, *40* (5), 2130-2140. DOI: 10.1016/j.jeurceramsoc.2019.12.045.

(12) Sekhar Tiwary, C.; Srivastava, C.; Kumbhakar, P. Onset of sphalerite to wurtzite transformation in ZnS nanoparticles. *Journal of Applied Physics* **2011**, *110* (3). DOI: 10.1063/1.3622625 (acccessed 6/11/2024).

(13) Dai, L.; Lesyuk, R.; Karpulevich, A.; Torche, A.; Bester, G.; Klinke, C. From Wurtzite Nanoplatelets to Zinc Blende Nanorods: Simultaneous Control of Shape and Phase in Ultrathin ZnS Nanocrystals. *The Journal of Physical Chemistry Letters* **2019**, *10* (14), 3828-3835. DOI: 10.1021/acs.jpclett.9b01466.

(14) Yu, J. H.; Joo, J.; Park, H. M.; Baik, S.-I.; Kim, Y. W.; Kim, S. C.; Hyeon, T. Synthesis of Quantum-Sized Cubic ZnS Nanorods by the Oriented Attachment Mechanism. *Journal of the American Chemical Society* **2005**, *127* (15), 5662-5670. DOI: 10.1021/ja044593f.

(15) Li, Y.; Li, X.; Yang, C.; Li, Y. Ligand-Controlling Synthesis and Ordered Assembly of ZnS Nanorods and Nanodots. *The Journal of Physical Chemistry B* **2004**, *108* (41), 16002-16011. DOI: 10.1021/jp0489018.
(16) Zhao, Y.; Zhang, Y.; Zhu, H.; Hadjipanayis, G. C.; Xiao, J. Q. Low-Temperature Synthesis of Hexagonal (Wurtzite) ZnS Nanocrystals. *Journal of the American Chemical Society* **2004**, *126* (22), 6874-6875. DOI: 10.1021/ja048650g.
(17) Ludi, B.; Olliges-Stadler, I.; Rossell, M. D.; Niederberger, M. Extension of the benzyl alcohol route to metal sulfides: "nonhydrolytic" thio sol–gel synthesis of ZnS and SnS2. *Chemical Communications* **2011**, *47* (18), 5280-5282. DOI: 10.1039/C1CC10856E.
(18) Thomson, J. W.; Nagashima, K.; Macdonald, P. M.; Ozin, G. A. From Sulfur−Amine Solutions to Metal Sulfide Nanocrystals: Peering into the Oleylamine−Sulfur Black Box. *Journal of the American Chemical Society* **2011**, *133* (13), 5036-5041. DOI: 10.1021/ja1109997.
(19) Joo, J.; Na, H. B.; Yu, T.; Yu, J. H.; Kim, Y. W.; Wu, F.; Zhang, J. Z.; Hyeon, T. Generalized and Facile Synthesis of Semiconducting Metal Sulfide Nanocrystals. *Journal of the American Chemical Society* **2003**, *125* (36), 11100-11105. DOI: 10.1021/ja0357902.
(20) Islam, H.-U.; Roffey, A.; Hollingsworth, N.; Bras, W.; Sankar, G.; De Leeuw, N. H.; Hogarth, G. Understanding the role of zinc dithiocarbamate complexes as single source precursors to ZnS nanomaterials. *Nanoscale Advances* **2020**, *2* (2), 798-807, 10.1039/C9NA00665F. DOI: 10.1039/C9NA00665F.
(21) Ströh, J.; Hess, T.; Ohrt, L.; Fritzsch, H.; Etter, M.; Dippel, A. C.; Nyamen, L. D.; Terraschke, H. Detailed insights into the formation pathway of CdS and ZnS in solution: a multi-modal in situ characterisation approach. *Physical Chemistry Chemical Physics* **2023**, *25* (6), 4489-4500, 10.1039/D2CP02707K. DOI: 10.1039/D2CP02707K.
(22) Zhai, X.; Zhang, X.; Chen, S.; Yang, W.; Gong, Z. Oleylamine as solvent and stabilizer to synthesize shape-controlled ZnS nanocrystals with good optical properties. *Colloids and Surfaces A: Physicochemical and Engineering Aspects* **2012**, *409*, 126-129. DOI: 10.1016/j.colsurfa.2012.05.047.
(23) Tzitzios, V.; Dimos, K.; Lelidis, I.; Boukos, N. K.; Wadi, V. S.; Basina, G.; Nounesis, G.; Alhassan, S. M. Sulfur–oleyl amine platelet derivatives with liquid crystalline behavior. *RSC Advances* **2018**, *8* (72), 41480-41483, 10.1039/C8RA08325H. DOI: 10.1039/C8RA08325H.
(24) Ramya, S.; Nataraj, D.; Krishnan, S.; Premkumar, S.; Thrupthika, T.; Sangeetha, A.; Senthilkumar, K.; Thangadurai, T. D. Aggregation induced emission behavior in oleylamine acetone system and its application to get improved photocurrent from In2S3 quantum dots. *Scientific Reports* **2020**, *10* (1), 19712. DOI: 10.1038/s41598-020-76703-0.
(25) McCubbin Stepanic, O.; Ward, J.; Penner-Hahn, J. E.; Deb, A.; Bergmann, U.; DeBeer, S. Probing a Silent Metal: A Combined X-ray Absorption and Emission Spectroscopic Study of Biologically Relevant Zinc Complexes. *Inorganic Chemistry* **2020**, *59* (18), 13551-13560. DOI: 10.1021/acs.inorgchem.0c01931.
(26) DeBeer, D. K. a. S. Application of Modern X-ray Spectroscopy in Chemistry—Beyond Studying the Oxidation State. *Chemistry of Materials* **2017**, *29* (17), 7051-7053. DOI: 10.1021/acs.chemmater.7b03455.
(27) Hirsch, O.; Kvashnina, K. O.; Luo, L.; Süess, M. J.; Glatzel, P.; Koziej, D. High-energy resolution X-ray absorption and emission spectroscopy reveals insight into unique selectivity of La-based nanoparticles for CO₂. *Proceedings of the National Academy of Sciences* **2015**, *112* (52), 15803-15808. DOI: doi:10.1073/pnas.1516192113.
(28) Glatzel, P.; Bergmann, U. High resolution 1s core hole X-ray spectroscopy in 3d transition metal complexes—electronic and structural information. *Coordination Chemistry Reviews* **2005**, *249* (1), 65-95. DOI: 10.1016/j.ccr.2004.04.011.

(29) Thomas, S. A.; Mishra, B.; Myneni, S. C. B. High Energy Resolution-X-ray Absorption Near Edge Structure Spectroscopy Reveals Zn Ligation in Whole Cell Bacteria. *The Journal of Physical Chemistry Letters* **2019**, *10* (10), 2585-2592. DOI: 10.1021/acs.jpclett.9b01186.
(30) Estevenon, P.; Amidani, L.; Bauters, S.; Tamain, C.; Bodensteiner, M.; Meurer, F.; Hennig, C.; Vaughan, G.; Dumas, T.; Kvashnina, K. O. From Molecular Oxo-Hydroxo Ce Clusters to Crystalline CeO2. *Chemistry of Materials* **2023**, *35* (4), 1723-1734. DOI: 10.1021/acs.chemmater.2c03456.
(31) Pollock, C. J.; DeBeer, S. Insights into the Geometric and Electronic Structure of Transition Metal Centers from Valence-to-Core X-ray Emission Spectroscopy. *Accounts of Chemical Research* **2015**, *48* (11), 2967-2975. DOI: 10.1021/acs.accounts.5b00309.
(32) Gallo, E.; Glatzel, P. Valence to Core X-ray Emission Spectroscopy. *Advanced Materials* **2014**, *26* (46), 7730-7746. DOI: 10.1002/adma.201304994.
(33) Bauer, M. HERFD-XAS and valence-to-core-XES: new tools to push the limits in research with hard X-rays? *Physical Chemistry Chemical Physics* **2014**, *16* (27), 13827-13837, 10.1039/C4CP00904E. DOI: 10.1039/C4CP00904E.
(34) Ravel, B.; Newville, M. ATHENA, ARTEMIS, HEPHAESTUS: data analysis for X-ray absorption spectroscopy using IFEFFIT. *Journal of Synchrotron Radiation* **2005**, *12* (4), 537-541. DOI: 10.1107/S0909049505012719.
(35) Grote, L.; Seyrich, M.; Döhrmann, R.; Harouna-Mayer, S. Y.; Mancini, F.; Kaziukenas, E.; Fernandez-Cuesta, I.; A. Zito, C.; Vasylieva, O.; Wittwer, F.; et al. Imaging Cu2O nanocube hollowing in solution by quantitative in situ X-ray ptychography. *Nature Communications* **2022**, *13* (1), 4971. DOI: 10.1038/s41467-022-32373-2.
(36) Grote, L.; Zito, C. A.; Frank, K.; Dippel, A.-C.; Reisbeck, P.; Pitala, K.; Kvashnina, K. O.; Bauters, S.; Detlefs, B.; Ivashko, O.; et al. X-ray studies bridge the molecular and macro length scales during the emergence of CoO assemblies. *Nature Communications* **2021**, *12* (1), 4429. DOI: 10.1038/s41467-021-24557-z.
(37) Gerber, E.; Romanchuk, A. Y.; Pidchenko, I.; Amidani, L.; Rossberg, A.; Hennig, C.; Vaughan, G. B. M.; Trigub, A.; Egorova, T.; Bauters, S.; et al. The missing pieces of the PuO2 nanoparticle puzzle. *Nanoscale* **2020**, *12* (35), 18039-18048, 10.1039/D0NR03767B. DOI: 10.1039/D0NR03767B.
(38) Yoko, A.; Omura, Y.; Ninomiya, K.; Nishibori, M.; Fujita, T.; Kasai, H.; Nishibori, E.; Chiba, N.; Seong, G.; Tomai, T.; et al. Fusion Growth and Extraordinary Distortion of Ultrasmall Metal Oxide Nanoparticles. *Journal of the American Chemical Society* **2024**, *146* (23), 16324-16331. DOI: 10.1021/jacs.4c05106.
(39) Hirsch, O.; Kvashnina, K.; Willa, C.; Koziej, D. Hard X-ray Photon-in Photon-out Spectroscopy as a Probe of the Temperature-Induced Delocalization of Electrons in Nanoscale Semiconductors. *Chemistry of Materials* **2017**, *29* (4), 1461-1466. DOI: 10.1021/acs.chemmater.6b05218.
(40) Kvashnina, K. O.; Kowalski, P. M.; Butorin, S. M.; Leinders, G.; Pakarinen, J.; Bès, R.; Li, H.; Verwerft, M. Trends in the valence band electronic structures of mixed uranium oxides. *Chemical Communications* **2018**, *54* (70), 9757-9760, 10.1039/C8CC05464A. DOI: 10.1039/C8CC05464A.
(41) Gilbert, B.; Frandsen, C.; Maxey, E. R.; Sherman, D. M. Band-gap measurements of bulk and nanoscale hematite by soft x-ray spectroscopy. *Physical Review B* **2009**, *79* (3), 035108. DOI: 10.1103/PhysRevB.79.035108.
(42) Liu, C.-Y.; Feng, P.; Ruotsalainen, K.; Bauer, K.; Decker, R.; Kusch, M.; Siewierska, K. E.; Pietzsch, A.; Haase, M.; Lu, Y.; et al. Role of La 5p in Bulk and Quantum-Confined Solids Probed

by the La 5p54f1 3D1 Excitonic Final State of Resonant Inelastic X-ray Scattering. *The Journal of Physical Chemistry C* **2023**, *127* (23), 11111-11118. DOI: 10.1021/acs.jpcc.3c02011.
(43) Suzuki, H.; Minola, M.; Lu, Y.; Peng, Y.; Fumagalli, R.; Lefrançois, E.; Loew, T.; Porras, J.; Kummer, K.; Betto, D.; et al. Probing the energy gap of high-temperature cuprate superconductors by resonant inelastic x-ray scattering. *npj Quantum Materials* **2018**, *3* (1), 65. DOI: 10.1038/s41535-018-0139-7.
(44) Cutsail Iii, G. E.; DeBeer, S. Challenges and Opportunities for Applications of Advanced X-ray Spectroscopy in Catalysis Research. *ACS Catalysis* **2022**, *12* (10), 5864-5886. DOI: 10.1021/acscatal.2c01016.
(45) Pankin, I. A.; Polozhentsev, O. E.; Soldatov, M. A.; Bugaev, A. L.; Tsaturyan, A.; Lomachenko, K. A.; Guda, A. A.; Budnyk, A. P.; Lamberti, C.; Soldatov, A. V. Investigation of the nanoscale two-component ZnS-ZnO heterostructures by means of HR-TEM and X-ray based analysis. *Journal of Solid State Chemistry* **2018**, *262*, 264-272. DOI: 10.1016/j.jssc.2018.03.008.
(46) Jaumot, J.; Gargallo, R.; de Juan, A.; Tauler, R. A graphical user-friendly interface for MCR-ALS: a new tool for multivariate curve resolution in MATLAB. *Chemometrics and Intelligent Laboratory Systems* **2005**, *76* (1), 101-110. DOI: 10.1016/j.chemolab.2004.12.007.
(47) de Juan, A.; Jaumot, J.; Tauler, R. Multivariate Curve Resolution (MCR). Solving the mixture analysis problem. *Analytical Methods* **2014**, *6* (14), 4964-4976, 10.1039/C4AY00571F. DOI: 10.1039/C4AY00571F.
(48) Rama Krishna, M. V.; Friesner, R. A. Quantum confinement effects in semiconductor clusters. *The Journal of Chemical Physics* **1991**, *95* (11), 8309-8322. DOI: 10.1063/1.461258 (acccessed 6/11/2024).
(49) Madelung, O. *Semiconductors: data handbook*; Springer Science & Business Media, 2004.
(50) Cárdenas, J. R.; Bester, G. Atomic effective pseudopotentials for semiconductors. *Physical Review B* **2012**, *86* (11), 115332. DOI: 10.1103/PhysRevB.86.115332.
(51) Zirkelbach, F.; Prodhomme, P. Y.; Han, P.; Cherian, R.; Bester, G. Large-scale atomic effective pseudopotential program including an efficient spin-orbit coupling treatment in real space. *Physical Review B* **2015**, *91* (7), 075119. DOI: 10.1103/PhysRevB.91.075119.
(52) Kumar, S.; Bui, H.; Bester, G. Empirical band-gap correction for LDA-derived atomic effective pseudopotentials. *Computational Condensed Matter* **2024**, *40*, e00917. DOI: 10.1016/j.cocom.2024.e00917.
(53) Karpulevich, A.; Bui, H.; Antonov, D.; Han, P.; Bester, G. Nonspherical atomic effective pseudopotentials for surface passivation. *Physical Review B* **2016**, *94* (20), 205417. DOI: 10.1103/PhysRevB.94.205417.
(54) Bester, G. Electronic excitations in nanostructures: an empirical pseudopotential based approach. *Journal of Physics: Condensed Matter* **2009**, *21* (2), 023202. DOI: 10.1088/0953-8984/21/2/023202.
(55) Karpulevich, A.; Bui, H.; Wang, Z.; Hapke, S.; Palencia Ramírez, C.; Weller, H.; Bester, G. Dielectric response function for colloidal semiconductor quantum dots. *The Journal of Chemical Physics* **2019**, *151* (22). DOI: 10.1063/1.5128334 (acccessed 7/24/2024).
(56) Koziej, D., Kopula Kesavan, J., Klemeyer, L., Rebber, M. N., Sani Harouna-Mayer, & Gröne, T. L. R. In situ photon-in photon-out spectroscopy measurements on ultra-small Cu3N nanoparticles. *European Synchrotron Radiation Facility* **2025**. DOI: 10.15151/ESRF-ES-657465136.
(57) Zito, C. D. A., Koziej, D., Caddeo, F., Kopula Kesavan, J., Klemeyer, L., Aaling-Frederiksen, O., Gröne, T. L. R., & Liu, X. Investigating the cooridnation of PtAg Nanoclusters in ZIF-8 by in situ HERFD-XANES studies. *European Synchrotron Radiation Facility* **2025**. DOI: 10.15151/ESRF-ES-819999907.

(58) Zito, C. D. A., Koziej, D., Kesavan, J. K., Klemeyer, L., Akcaalan, M. G., Hussak, S.A., & Gröne, T. L. R. in situ photon-in-photon-out spectroscopic studies with high temporal, spatial and energy resolution during emergence of transition metal su. *European Synchrotron Radiation Facility* **2026**. DOI: 10.15151/ESRF-ES-1022934512.
(59) Derelli, D.; Frank, K.; Grote, L.; Mancini, F.; Dippel, A.-C.; Gutowski, O.; Nickel, B.; Koziej, D. Direct Synthesis of CuPd Icosahedra Supercrystals Studied by In Situ X-Ray Scattering. *Small n/a* (n/a), 2311714. DOI: 10.1002/smll.202311714.
(60) Staniuk, M.; Hirsch, O.; Kränzlin, N.; Böhlen, R.; van Beek, W.; Abdala, P. M.; Koziej, D. Puzzling Mechanism behind a Simple Synthesis of Cobalt and Cobalt Oxide Nanoparticles: In Situ Synchrotron X-ray Absorption and Diffraction Studies. *Chemistry of Materials* **2014**, *26* (6), 2086-2094. DOI: 10.1021/cm500090r.
(61) Makuła, P.; Pacia, M.; Macyk, W. How To Correctly Determine the Band Gap Energy of Modified Semiconductor Photocatalysts Based on UV–Vis Spectra. *The Journal of Physical Chemistry Letters* **2018**, *9* (23), 6814-6817. DOI: 10.1021/acs.jpclett.8b02892.
(62) Derelli, D.; Caddeo, F.; Frank, K.; Krötzsch, K.; Ewerhardt, P.; Krüger, M.; Medicus, S.; Klemeyer, L.; Skiba, M.; Ruhmlieb, C.; et al. Photodegradation of CuBi2O4 Films Evidenced by Fast Formation of Metallic Bi using Operando Surface-sensitive X-ray Scattering. *Angewandte Chemie International Edition* **2023**, *62* (43), e202307948. DOI: 10.1002/anie.202307948.
(63) Haas, S.; Sun, X.; Conceicao, A. L. C.; Horbach, J.; Pfeffer, S. The new small-angle X-ray scattering beamline for materials research at PETRA III: SAXSMAT beamline P62. *Journal of Synchrotron Radiation* **2023**, *30* (6), 1156-1167. DOI: 10.1107/S1600577523008603.
(64) Newville, M. Larch: An Analysis Package for XAFS and Related Spectroscopies. *Journal of Physics: Conference Series* **2013**, *430* (1), 012007. DOI: 10.1088/1742-6596/430/1/012007.
(65) Harris, C. R.; Millman, K. J.; van der Walt, S. J.; Gommers, R.; Virtanen, P.; Cournapeau, D.; Wieser, E.; Taylor, J.; Berg, S.; Smith, N. J.; et al. Array programming with NumPy. *Nature* **2020**, *585* (7825), 357-362. DOI: 10.1038/s41586-020-2649-2.
(66) Virtanen, P.; Gommers, R.; Oliphant, T. E.; Haberland, M.; Reddy, T.; Cournapeau, D.; Burovski, E.; Peterson, P.; Weckesser, W.; Bright, J.; et al. SciPy 1.0: fundamental algorithms for scientific computing in Python. *Nature Methods* **2020**, *17* (3), 261-272. DOI: 10.1038/s41592-019-0686-2.
(67) Neese, F. Software update: The ORCA program system—Version 5.0. *WIREs Computational Molecular Science* **2022**, *12* (5), e1606. DOI: 10.1002/wcms.1606.
(68) Hanwell, M. D.; Curtis, D. E.; Lonie, D. C.; Vandermeersch, T.; Zurek, E.; Hutchison, G. R. Avogadro: an advanced semantic chemical editor, visualization, and analysis platform. *Journal of Cheminformatics* **2012**, *4* (1), 17. DOI: 10.1186/1758-2946-4-17.
(69) Kieffer, J.; Wright, J. P. PyFAI: a Python library for high performance azimuthal integration on GPU. *Powder Diffraction* **2013**, *28* (S2), S339-S350. DOI: 10.1017/S0885715613000924 From Cambridge University Press Cambridge Core.
(70) Toby, B. H.; Von Dreele, R. B. GSAS-II: the genesis of a modern open-source all purpose crystallography software package. *Journal of Applied Crystallography* **2013**, *46* (2), 544-549. DOI: 10.1107/S0021889813003531.
(71) *SASView webpage*. https://www.sasview.org (accessed 2023 05.10.2023).
(72) Vrugt, J. A.; Ter Braak, C. J. F. DREAM_(D): an adaptive Markov Chain Monte Carlo simulation algorithm to solve discrete, noncontinuous, and combinatorial posterior parameter estimation problems. *Hydrol. Earth Syst. Sci.* **2011**, *15* (12), 3701-3713. DOI: 10.5194/hess-15-3701-2011.

(73) Buriak, J. M.; Akinwande, D.; Artzi, N.; Brinker, C. J.; Burrows, C.; Chan, W. C. W.; Chen, C.; Chen, X.; Chhowalla, M.; Chi, L.; et al. Best Practices for Using AI When Writing Scientific Manuscripts. *ACS Nano* **2023**, *17* (5), 4091-4093. DOI: 10.1021/acsnano.3c01544.

For Table of Content Only